Available online at www.sciencedirect.com
ScienceDirect
Trans. Nonferrous Met. Soc. China 35(2025) 225−242
Transactions of Nonferrous Metals Society of China
www.tnmsc.cn

Flow behavior and dynamic softening mechanism of Pt−10Ir precious alloy

Xin-pei ZHANG[1], Jun-jie HE[1], Lin PI[1], Quan FU[2], Wen-yan ZHOU[3,4], Jun CHENG[5], Sheng-wen BAI[6], Xuan ZHOU[1], Yi LIU[2], Yong MAO[1]

1. Materials Genome Institute, School of Materials and Energy, Yunnan University, Kunming 650091, China;
2. Kunming Precious Materials & Technology Co., Ltd., Yunnan Precious Metals Laboratory Co. Ltd., Sino-Platinum Metals Co. Ltd., Kunming 650106, China;
3. Kunming Institute of Precious Metals, Kunming 650106, China;
4. State Key Laboratory of Advanced Technologies for Comprehensive Utilization of Platinum Metals, Sino-Platinum Metals Co., Ltd., Kunming 650106, China;
5. Shaanxi Key Laboratory of Biomedical Metal Materials, Northwest Institute for Non-ferrous Metal Research, Xi'an 710016, China;
6. College of Materials Science and Engineering, Chongqing University, Chongqing 400044, China

Received 6 June 2023; accepted 30 December 2023

Abstract: The hot deformation behavior of Pt−10Ir alloy was studied under a wide range of deformation parameters. At a low deformation temperature (950−1150 °C), the softening mechanism is primarily dynamic recovery. In addition, dynamic recrystallization by progressive lattice rotation near grain boundaries (DRX by LRGBs) and microshear bands assisted dynamic recrystallization (MSBs assisted DRX) coordinate the deformation. However, it is difficult for the dynamic softening to offset the stain hardening due to a limited amount of DRXed grains. At a high deformation temperature (1250−1350 °C), three main DRX mechanisms associated with strain rates occur: DRX by LRGBs, DRX by a homogeneous increase in misorientation (HIM) and geometric DRX (GDRX). With increasing strain, DRX by LRGBs is enhanced gradually under high strain rates; the "pinch-off" effect is enhanced at low strain rates, which was conducive to the formation of a uniform and fine microstructure.

Key words: platinum alloy; hot deformation; microstructure evolution; dynamic recovery; dynamic recrystallization

1 Introduction

Pt−10Ir alloy is a typical platinum−iridium alloy with ultrahigh corrosion resistance, good machining performance and excellent electrical performance [1,2]. This alloy is widely used in sophisticated aerospace equipment, national defense and military industry, for materials such as bonding wires and electrical contact elements. However, wire breakage easily occurs in the process of bonding wire drawing, and the performance stability of electrical contact cannot meet the needed level. The main reason for the above problems is that the processing mechanism of cast Pt−10Ir alloy is unclear. Bonding wires require hot working during processing, but the relationship between the selection of hot working parameters and the evolution mechanism of the microstructure is relatively unclear. Therefore, understanding the

Corresponding author: Jun-jie HE, Tel: +86-13340356562, E-mail: 20210015@ynu.edu.cn;
Yong MAO, Tel: +86-13888319162, E-mail: maoyong@ynu.edu.cn
https://doi.org/10.1016/S1003-6326(24)66676-8

flow behavior, and optimizing the microstructure during hot working are crucial for production and excellent performance.

At present, hot deformation behavior has rarely been reported in Pt−10Ir alloys. Isothermal hot compression has been applied to exploring the hot deformation characteristics of many metals. The method explores the influence of different deformation temperatures and strain rates on microstructure by controlling variables, providing a reference for optimizing actual hot working parameters. This method has been applied in the study of hot deformation of many alloys. Using isothermal unidirectional compression, GUI et al [3] investigated the effect of the thermomechanical processing parameters on the dynamic softening mechanism of Mg−4Y−2Nd−1Sm−0.5Zr alloys. They found that the softening mechanism translated from the synergy of discontinuous dynamic recrystallization (DDRX) and continuous dynamic recrystallization (CDRX) at a high temperature. At low temperatures, the dynamic recrystallization (DRX) process is weak, and deformation twins can provide sites for DDRX and CDRX. Compared with CDRX, DDRX includes a nucleation process, and DDRX relies on strain-induced grain boundary migration (SIBM) [4]. YIN et al [5] found that CDRX is the dominant recrystallization mechanism under all deformation conditions of the studied 50Ti−47Ni−3Fe alloy, and the migration of HAGBs could be considered a secondary mechanism at a low temperature or a high strain rate, so the true strain–true stress curves show an insignificant downward trend. CHAMANFAR et al [6] found that the main flow softening mechanism of homogenized AA6099 is dynamic recovery (DRV), and partial DRX enhances dynamic softening, especially at low deformation temperatures and high strain rates. The amount of DRX is enhanced to some extent at low temperatures and high strain rates, a combination of DDRX, CDRX and geometric dynamic recrystallization (GDRX) participates in the development of DRX grains, GDRX is the dominant DRX mechanism for the formation of block-like grains, and CDRX makes the transformation of low angle grain boundaries (LAGBs) to high angle grain boundaries (HAGBs) more obvious. Similar results were found by LI et al [7] during the study of Al−Mg−Si alloys, dynamic recovery can facilitate CDRX which relies on subgrain progressive rotation, and GDRX can be facilitated through intensive DRV at the marge region of the initial grain boundary. Although GDRX is considered one type of CDRX, it is justified that GDRX has many different features from CDRX, especially the grain morphology, which is particularly crucial to GDRX [8]. Some mechanisms may have a positive impact on DRX; for example, as the deformation temperature decreases, the kinetics of microstructure evolution decelerates, and the microbands and deformation bands formed by strain localization are enhanced, which promotes the formation of ultrafine grains during hot rolling in 304-type austenitic stainless steel [9].

The above studies on the hot working of different alloys were focused on the theory of hot deformation, and provided a reference for the formulation of hot working parameters. However, the dynamic softening mechanism of high stacking alloys (such as the studied Pt−10Ir alloy) may be very different. Although research based on other alloys can provide a reference for exploring the hot working of Pt−10Ir alloys, it is still necessary to explore the microstructure evolution of Pt−10Ir alloys under different conditions to guide the production.

The focus of this study is the mechanism of hot deformation because of the increasing demand of enterprises for the quality and quantity of Pt−10Ir products. Isothermal compression was used to investigate the flow behavior and microstructure evolution during the hot working process. The dynamic softening mechanism was studied to provide theoretical guidance for the hot working of Pt−10Ir alloy, especially the correlation between the deformation process of different DRX mechanisms and temperatures, strain rates and strains.

2 Experimental

The studied Pt−10Ir alloy was provided by Sino-Precious Metals Co., Ltd., Kunming, China. Cylindrical specimens with dimensions of 6 mm in diameter and 9 mm in height were cut from the casting billet for isothermal compression. Before hot compression, the specimens underwent a homogenization treatment at 950 °C for 5 h and were then cooled by water quenching.

Isothermal compression tests were performed

on a Gleeble–3800 thermomechanical simulator. The hot compression tests were carried out at an individual strain of 0.7, five different hot compression temperatures (950, 1050, 1150, 1250, and 1350 °C), and four different strain states (0.001, 0.01, 0.1 and 1 s^{-1}). Then, the hot compression tests were carried out at different temperatures (1150 and 1350 °C), two strain rates (0.01 and 1 s^{-1}), and three true strains (0.35, 0.7, 1.05). To minimize the friction between the specimen and the dies, a tantalum foil was used between the dies and the specimen surface. The specimen was heated to the designed temperature at a heating rate of 10 °C/s and held for 180 s to ensure uniform temperature distribution. After hot compression, the samples were instantly cold water-quenched. Specimens for electron backscattered diffraction (EBSD) were prepared by standard mechanical polishing and finished by a cross section-polisher (PECS II). EBSD observations were carried out using a dual-beam scanning electron microscope (TESCAN AMBER) equipped with an EBSD camera. The compressed specimens were sectioned parallel to the compression axis along the direction of the centerline for EBSD observation. Transmission electron microscopy (TEM) specimens were prepared by focused ion beam (FIB, Thermo Fisher Helios 5 CX), and submicrostructures were obtained using a Talos F200X microscope operated at 200 kV.

3 Results and discussion

3.1 Initial microstructure

The optical microscope (OM) photograph and inverse pole figures (IPF) map of the Pt−10Ir alloy after solution treatment are shown in Figs. 1(a, b). The initial microstructure consists of relatively uniform equiaxed grains, and a weak-textured microstructure can be observed in Fig. 1(c).

3.2 Flow behavior evolution

The true stress–true strain curves of the Pt−10Ir alloy at different temperatures and strain rates are shown in Fig. 2. The hot deformation temperature and strain rate have significant effects on the flow characteristics of this alloy. The flow stress decreases remarkably with increasing temperature and decreasing strain rate. There are roughly two stages in the true stress–true strain curves: the work-hardening region and the relative steady-state flow stress region. The true stress increases sharply in the initial deformation stage. The variation in true stress with true strain is caused

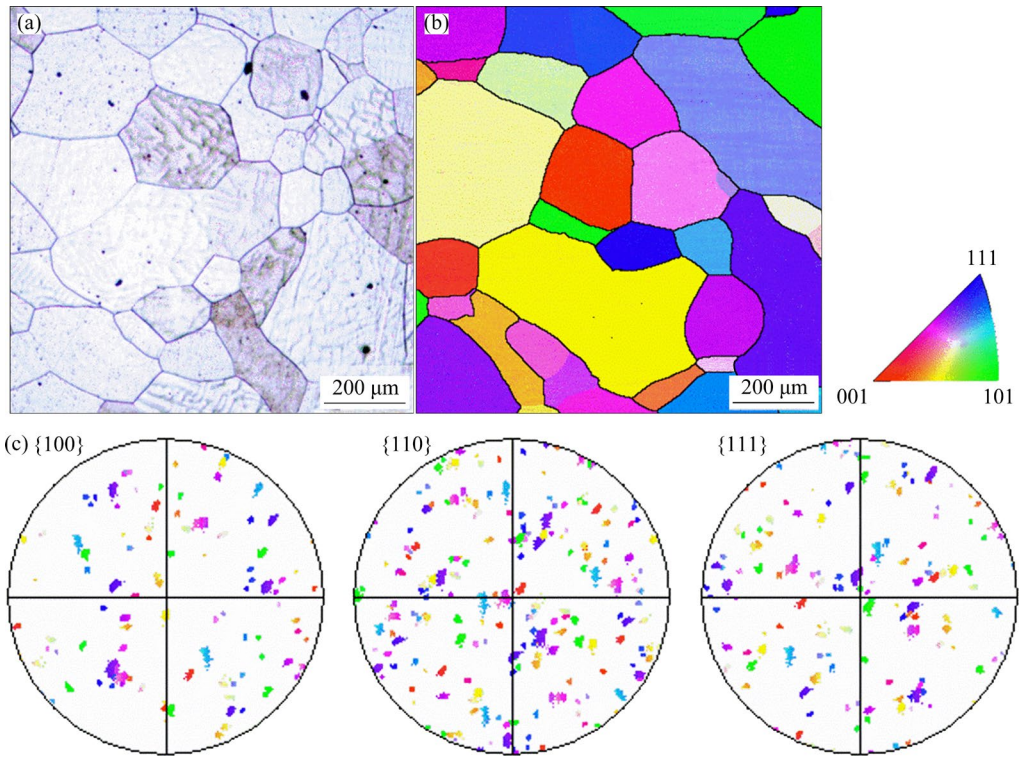

Fig. 1 Microstructure of Pt−10Ir alloy before hot compression: (a) OM image; (b) IPF map; (c) Corresponding pole figures of {100}, {110}, and {111}

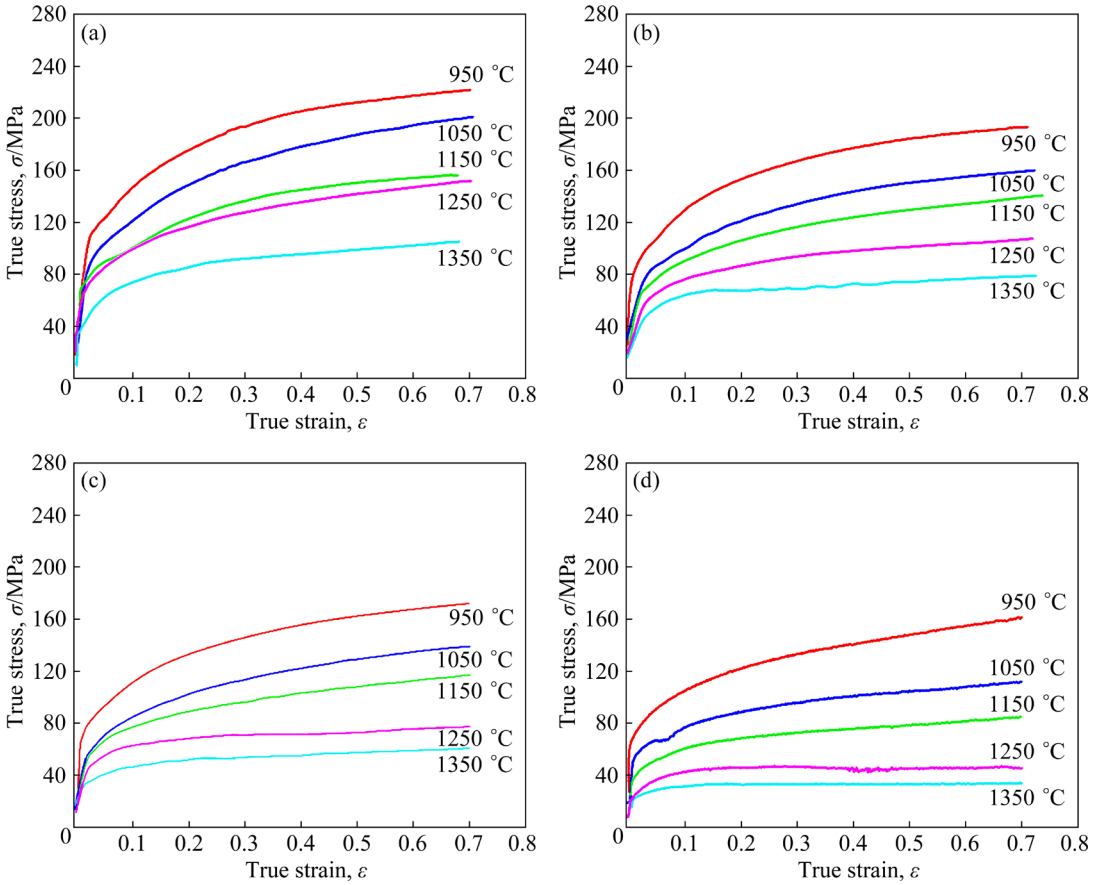

Fig. 2 True stress−true strain curves obtained by isothermal compression tests of Pt−10Ir samples at 950−1350 °C and different strain rates: (a) 1 s^{-1}; (b) 0.1 s^{-1}; (c) 0.01 s^{-1}; (d) 0.001 s^{-1}

by rapid dislocation multiplication and accumulation. The dislocations generated by hot deformation entangle each other and hinder the corresponding dislocation movement, and a work-hardening region appears [10−12].

The weak strain softening is mainly caused by the DRV process with rapidly increasing strain after the work-hardening region. Dynamic softening is enhanced by dislocation annihilation, which can offset or partially offset the work-hardening effect [13,14]. As the true strain is further increased, the true stress does not change obviously in a relatively wide strain range in the relative steady-state region. The true stress−true strain curve remains unchanged or increases slightly at high temperature (1250 and 1350 °C) and low strain rate (0.001 and 0.01 s^{-1}). Many curves show an upward trend at low temperatures (950, 1050 and 1150 °C) or high strain rates (1 s^{-1}). This is because the effect of work-hardening is high. However, there is no obvious warping on those curves with upward trend, and the true stress only increases slightly with increasing true strain. Dynamic softening occurs at low temperatures and high strain rates, but the effect of DRX and DRV cannot completely offset the impact of work hardening [15].

3.3 Microstructure deformed at low temperature (950−1150 °C)

Figure 3 shows the microstructure of Pt−10Ir alloy deformed at relatively lower temperatures (950−1150 °C). The true stress−true strain curves at 950−1150 °C in Fig. 2 exhibit the characteristics of constant hardening. The microstructures are similar and characterized by a large amount of initial deformed grains and a small amount of dynamic recrystallized grains around and inside deformed grains. Many deformation bands in the initial grains (marked by arrows in Figs. 3(a, b) and surrounded by yellow box A in Fig. 3(c)) are easily observed at low deformation temperatures or high strain rates. Some necklace structures can be observed along the grain boundaries at low strain rates, as shown in Fig. 3(e) (marked by yellow box B).

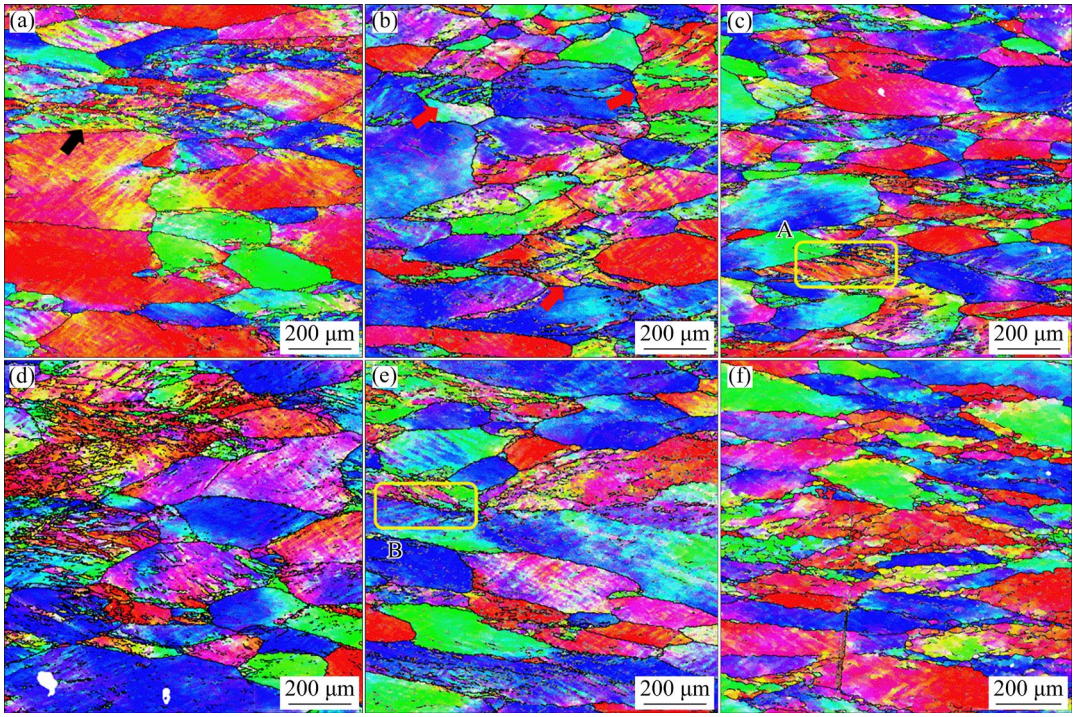

Fig. 3 IPF maps of Pt−10Ir alloy deformed at low temperatures: (a) 950 °C, 0.01 s^{-1}; (b) 1050 °C, 0.01 s^{-1}; (c) 1150 °C, 1 s^{-1}; (d) 1150 °C, 0.1 s^{-1}; (e) 1150 °C, 0.01 s^{-1}; (f) 1150 °C, 0.001 s^{-1} (Gray lines are middle angle grain boundaries (MAGBs) with misorientation between 10° and 15°, and black lines are high angle grain boundaries (HAGBs) with misorientation higher than 15°)

To systematically discuss the effect of the deformation bands, case of 1150 °C, 1 s^{-1} is chosen for a detailed analysis. At a low deformation temperature of 1150 °C and a high strain rate of 1 s^{-1}, some microbands (consisting of LAGBs and MAGBs) and deformation bands (consisting of HAGBs) can be observed in Fig. 4 (the region surrounded by yellow box A in Fig. 3(c)). Some subgrains and DRX grains are generated between deformation bands. To explore the formation mechanism of these DRX grains, four randomly picked grains in the deformation band are selected from Zone I to analyze the point-to-origin misorientation (cumulative misorientation), and the corresponding orientation gradients are shown in Fig. 5(a).

As shown in Fig. 5(a), the cumulative misorientation increases rapidly to nearly 14° within 8 μm, indicating that a high dislocation density exists in Grains 1, 3 and 4. The cumulative misorientation of Grain 2 is 2°−4° within 6 μm, indicating that the dislocations in Grain 2 may be used for the transformation from LAGBs into HAGBs. The four randomly picked grains are different from DDRX grains with inside cumulative misorientation below 1° [16].

Figure 5(b) shows the orientation gradient measured by Lines 1, 2, 3, and 4 in Fig. 4. The misorientation between the deformation band and initial grain of Zone III is approximately 45°−55°, as shown in Line 1 and Line 2. The misorientation between the microbands is 8°−15° in Zone IV. The cumulative misorientation between the microband is smaller than that between the deformation bands, and it can be found that most parts of the microband in Zone IV are composed of LAGBs, and some MAGBs and HAGBs exist in some parts, as shown in the black circles in Zone IV. Since LAGB and MAGB are types of geometrically necessary subboundary, the misorientation increases sharply upon hot deformation, resulting in their conversion to HAGBs [17−19]. Therefore, the microbands in Zone IV eventually transform into deformation bands if the hot deformation process continues.

Deformation bands are beneficial to the generation of fine-grained structures. Some fine-grained DRX grains are separated from the deformation

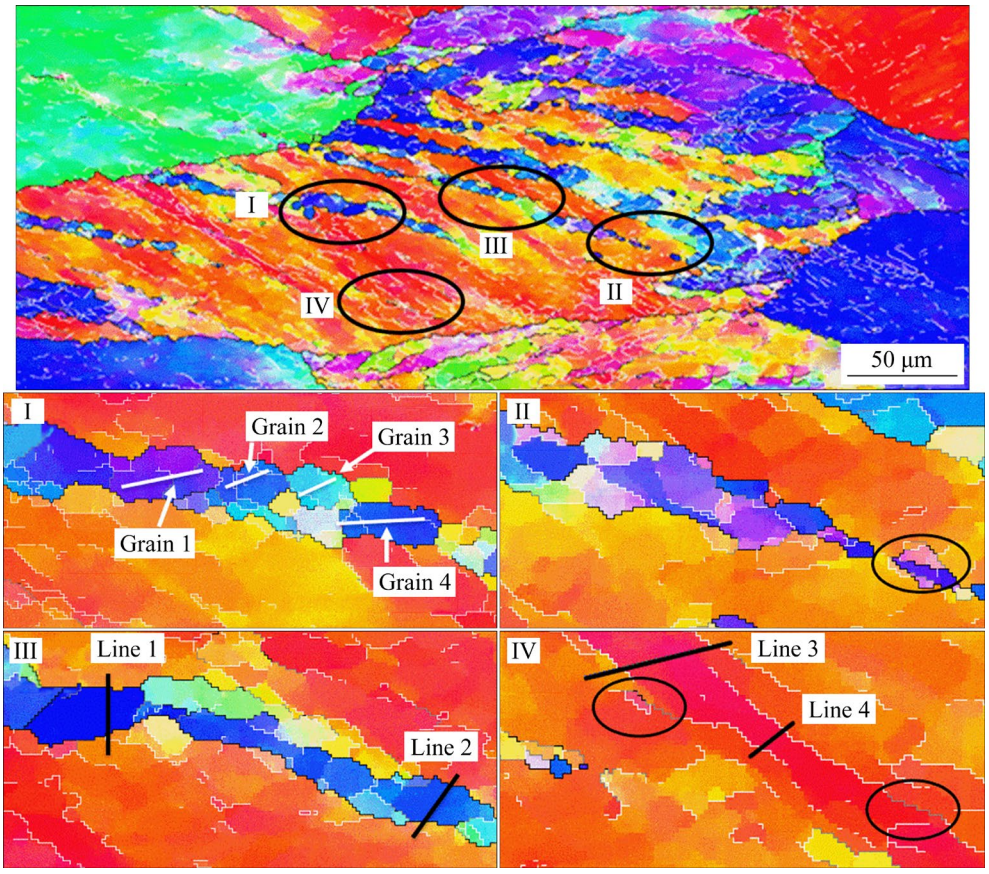

Fig. 4 Magnified IPF map of deformation bands and microbands in Fig. 3(c) (Gray lines are MAGBs, black lines are HAGBs, and white lines are LAGBs with misorientation between 2° and 10°)

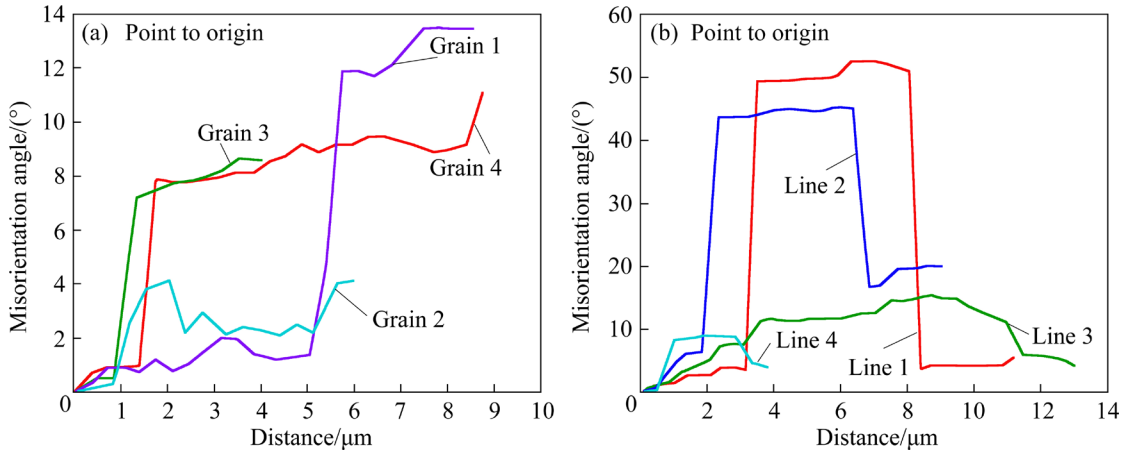

Fig. 5 Orientation gradient (a) measured in Grains 1, 2, 3 and 4 of Zone I in Fig. 4; orientation gradient (b) measured by Lines 1, 2, 3, and 4 of Zones III and IV in Fig. 4

band in Zone II of Fig. 4. This is mainly due to the existence of strain-induced grain boundaries perpendicular to the extension direction. These strain-induced subboundaries subdivide preexisting microbands and deformation bands into chains of subgrains, and the misorientation of those subgrains increases and results in the evolution of ultrafine grains with increasing strain [9].

To further study the influence of the deformation band on the evolution of the microstructure, TEM analysis was used on the samples deformed at 1150 °C, 1 s^{-1}, and the TEM sample was extracted from an area perpendicular to the deformation band, as shown in Fig. 6(a).

The TEM micrograph (Fig. 6(b)) shows the deformation band area in the sample deformed at

1150 °C, 1 s^{-1}, as marked by the white dashed line. Figure 6(c) shows the magnified region marked in Fig. 6(b). The deformation band (marked by white dashed lines) contains a DRX region with low-density dislocation and a deformation region with high-density dislocations. The deformation region in the deformation band shows that a cell structure is formed at high-density dislocations, and some dislocation walls can be found due to dislocation motion and rearrangement. Dislocation walls divide the deformation band into several parts, which can be regarded as precursors of DRX grains generated in the deformation band, and the result clearly reveals that this DRX mechanism has no recognizable nucleation and growth. The mechanism of deformation bands assisted DRX could be seen as a type of mechanism of microshear bands assisted DRX (MSBs assisted CDRX). A similar DRX mechanism can also occur in duplex stainless steel: strain tends to distribute in the interphase because the hardness of austenite and ferrite are different, and the parts of austenite regions near the interphase accommodate most of the strain, which facilitates the formation of MSBs and deformation bands. The transition regions of MSBs and deformation bands are the dominant softening mechanism in the phase where DRX is difficult to occur [20,21].

The microbands and deformation bands are formed by intense strain localization, which results from an insufficient softening effect at a low deformation temperature. The evolution of those band-like structures followed by DRV leads to subdivision and grain refinement during hot deformation.

3.4 Microstructure deformed at high temperature (1250−1350 °C)

Figure 7 shows the IPF maps of the specimens deformed at high temperature (1250−1350 °C). More subboundaries and DRX grains can be observed at a high strain rate of 1 s^{-1}, and necklace structures, microbands and deformation bands can also be observed in the microstructure, as shown in Figs. 7(a, c).

With a decrease in the strain rate (Figs. 7(c−f)), more cell structures can be observed, and the size of the new DRX grains is larger than that deformed at low temperature because increasing the deformation time allows sufficient time for the newly formed DRX grains to grow. Compared with the specimens deformed at the high strain rate, the initial grains deformed at the lower strain rates of 0.01 and 0.001 s^{-1} have noticeable dynamic softening, uniform deformation and noticeable flattening. The initial grain boundaries are plastically elongated perpendicular to the deformation direction. The microstructure deformed at high temperature and low strain rate exhibits obvious characteristics of DRV, which is consistent with the true stress–true strain curves.

Three characteristic regions are selected to discuss the mechanism of microstructure evolution at a high temperature of 1350 °C and a high strain rate of 1 s^{-1} (Regions C, D, and E marked by yellow boxes in Fig. 7(c)). A duplex microstructure can be observed, which consists of (1) initial grains, i.e., large deformed grains containing substructures and (2) fine equiaxed grains surrounded by HAGBs formed on the grain boundaries or on/near the deformation bands.

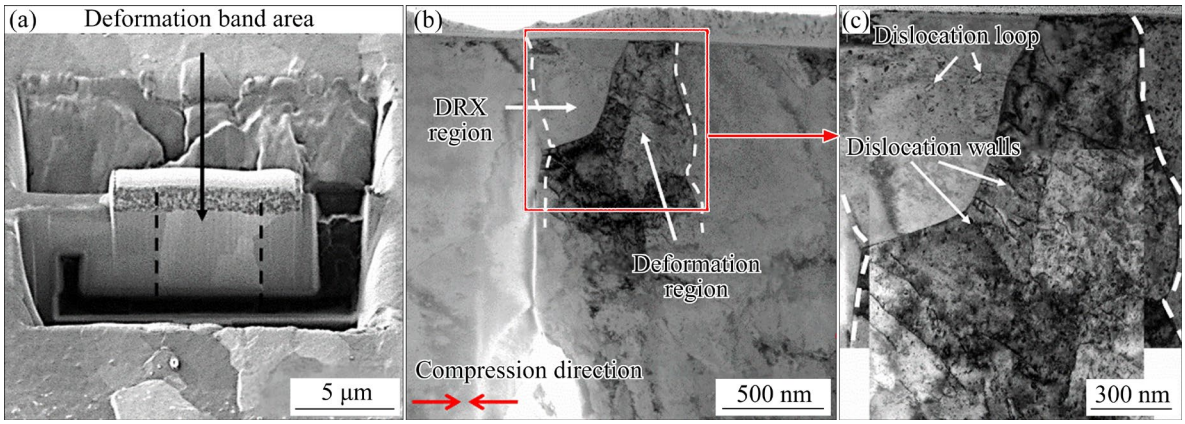

Fig. 6 Deformation substructure near deformation band in sample deformed at at 1150 °C, 1 s^{-1} (The area marked with white dashed lines represents the cross-section of the deformation band)

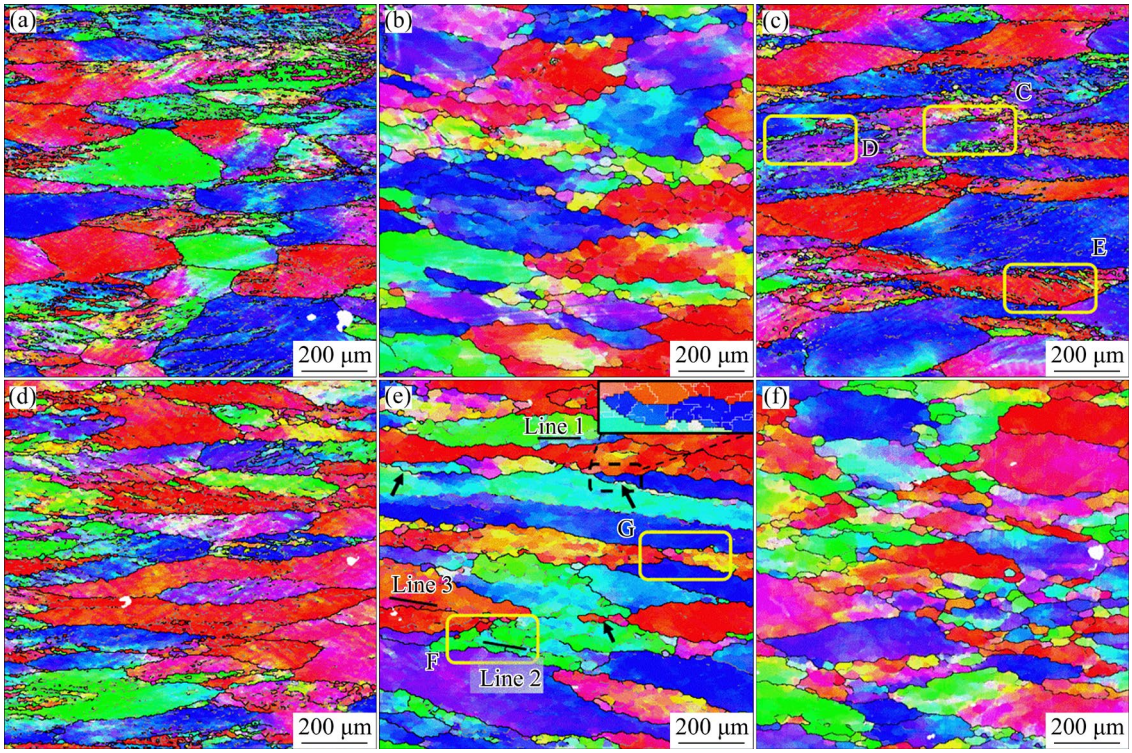

Fig. 7 IPF maps at high deformation temperatures: (a) 1250 °C, 1 s^{-1}; (b) 1250 °C, 0.001 s^{-1}; (c) 1350 °C, 1 s^{-1}; (d) 1350 °C, 0.1 s^{-1}; (e) 1350 °C, 0.01 s^{-1}; (f) 1350 °C, 0.001 s^{-1}

The initial grain boundaries become serrated and bulged, as presented in Fig. 8(a). As a typical symbol of DDRX, serrated grain boundaries (GBs) and bulging are important nucleation sites for DRX, as indicated by red arrows. Necklace structures can be observed around the initial grain boundaries in Figs. 8(a, b), but these necklace structures do not seem to be entirely formed by DDRX because there are numerous substructures within the necklace structures.

Figure 8(c) shows the kernel average misorientation (KAM) map of the area marked with a black box in Fig. 8(a). The KAM map is applied to describing the dislocation density or strain concentration. Grain 1 and Grain 2 in Fig. 8(c) are typical DRX grain nuclei of DDRX, and the initial grain boundaries tend to move toward the region with high dislocation density; nevertheless, intense DRV reduces the dislocation density to a low level, so the DDRX progress characterized by SIBM is obstructed. The necklace structure is regarded as the main feature of DDRX, as reported previously [16]. However, it is unreasonable to attribute the necklace structure initiated through SIBM for alloys to high stacking fault energy (SFE); there must be other mechanisms that contribute to the formation of necklace structures during hot deformation.

Figure 8(d) shows the KAM map of the region marked with a black box in Fig. 8(b). The necklace structure is surrounded by HAGBs completely, and many subgrains in the necklace structure have remnant strain concentrations and substructures (LAGBs and MAGBs). The necklace structure in Fig. 8(a) has more comprehensive development characteristics, so it can be considered the precursor of the necklace structure in Fig. 8(b). The external HAGBs are preferentially formed, and then the internal part is separated by subboundaries. For example, Grain 3, as a serrated part, is separated from the necklace structure.

The DRX grains are generated not only at the edge of the initial grain boundaries but also inside the initial grains (such as Grain 4). In places far from the initial grain boundaries, some strain-induced grain boundaries (marked by black arrows in Fig. 8(b)) as well as many subgrains in irregular shapes are enclosed or semienclosed by LAGBs and MAGBs. The DRX gradually extends from the initial grain boundary to the interior.

Two regions are selected (labeled with red boxes in Fig. 8(c)) to investigate the influence of subgrains near the initial grain boundary on DRX

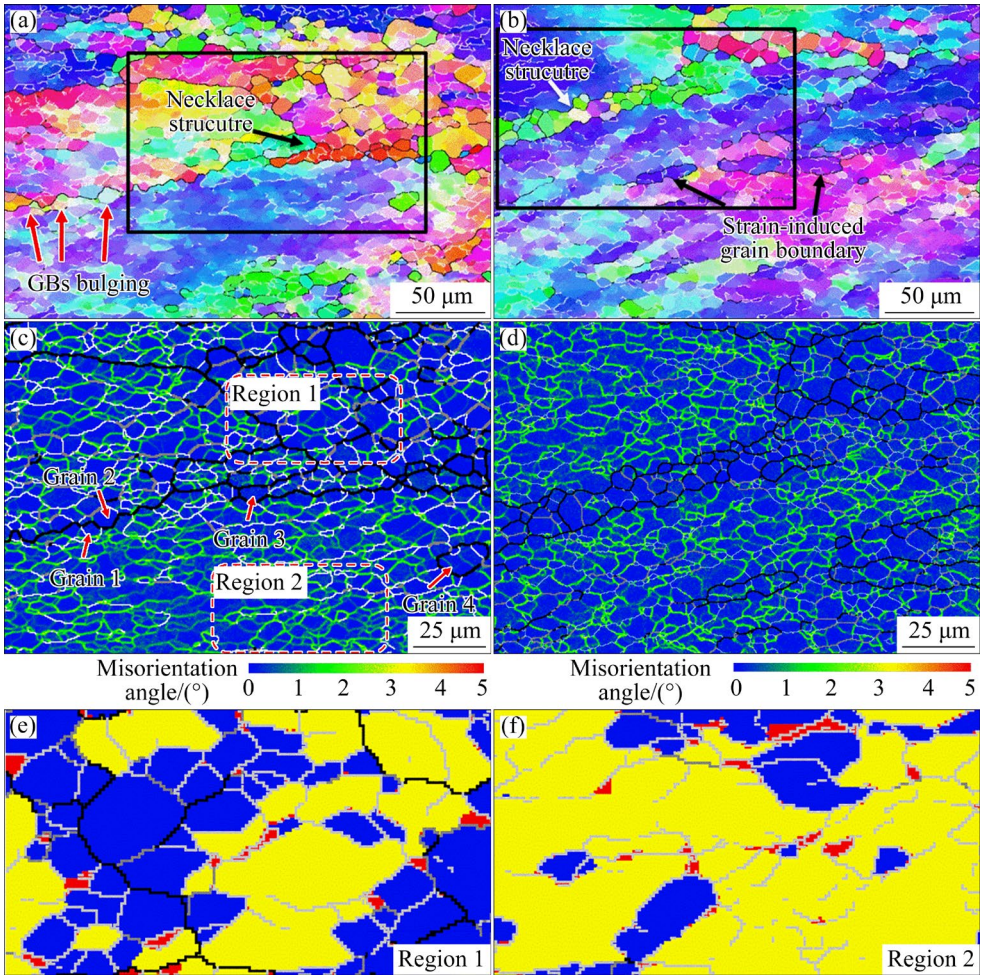

Fig. 8 Magnified Regions C (a) and D (b) in Fig. 7(c) of sample deformed at 1350 °C, 1 s^{-1}; KAM maps marked by black box (c) in (a) and black box (d) in (b); GOS maps of Regions 1 (e) and 2 (f) in (c)

behavior. The grain orientation spread (GOS) map is used as an indicator of the degree of DRX, separating the recrystallized grains (GOS≤1°−2°) and subgrains (GOS≤7°) from the initially deformed grains. The blue parts in the GOS map indicate the recrystallized grains, the yellow parts indicate the subgrains, and the red parts indicate the deformed grains. The grains near the initial grain boundaries are well developed, as shown in Fig. 8(e), while the internal region has higher GOS values, as shown in Fig. 8(f). The subgrains in Fig. 8(e) can develop into DRX completely in advance, especially near the initial grain boundaries.

The TEM observations in Fig. 9 reveal that the firstly formed dislocation walls frequently tend to align along the grain boundaries, and some dislocation walls divide the margin region into several subgrains near the initial grain boundaries. In high SFE alloys, dislocation cells and LAGBs tend to form near the initial grain boundaries, and these substructures form smaller brick-like subgrains to promote DRX. This kind of DRX mechanism depends on the subgrains generated at the edge of the initial grains [7,22]. In addition, the dislocation networks located inside the initial grain form subgrain boundaries by continuously absorbing surrounding free dislocations. The dislocation network formed by LAGBs can easily develop with the effect of dislocation rearrangements by cross-slip and climb, and those strain-induced subgrains could serve as precursors of DRX grains. The formation mechanism of the new grains is that LAGBs absorb dislocation energy to form subgrain boundaries to divide the initial grains [23,24].

At different deformation temperatures, necklace structures are formed at the initial grain boundaries, but the formation mechanism of these necklace structures is different. To explore the

formation mechanism of the necklace structure at different hot deformation temperatures, the necklace structures near the initial grain boundaries at 1150 °C, 0.01 s^{-1} (Fig. 10(a)) and 1350 °C, 1 s^{-1} (Fig. 10(b)) are compared.

There are two typical modes of the misorientation profile within the necklace structure of Figs. 10(c, d), as shown in Fig. 11: (1) The point-to-point misorientations along Line 1 and Line 2 in Fig. 10(c) oscillate up and down between 1°, while the point-to-origin misorientations along Line 1 and Line 2 exceed 4° within a short distance, showing a large progressive lattice rotation from the grain center to the grain boundary and a limited structural rearrangement in these grains, as shown in Figs. 11(a, b); (2) Both point-to-point and cumulative misorientations along Line 3 and Line 5 in Fig. 10(d) oscillate below 1°, implying that there is no obvious accumulation of misorientation in those new grains, as shown in Figs. 11(c, e), while the mode of Line 4 in Fig. 10(d) is similar to that of Line 1 and Line 2, as shown in Fig. 11(d).

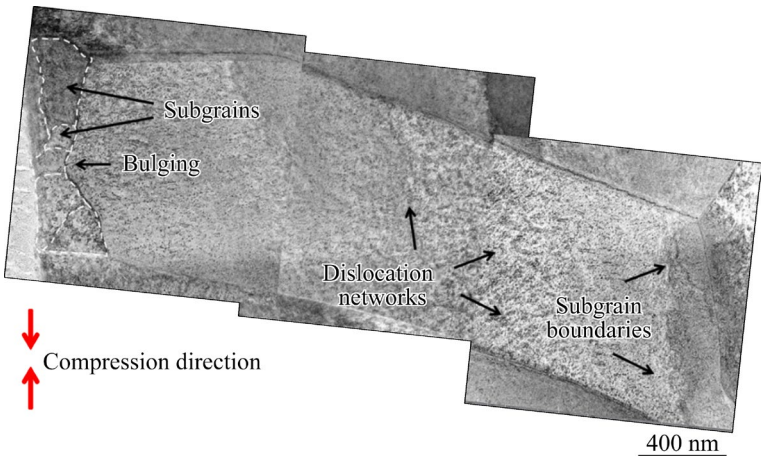

Fig. 9 Deformation substructure of deformed grain in specimen deformed at 1350 °C, 1 s^{-1}

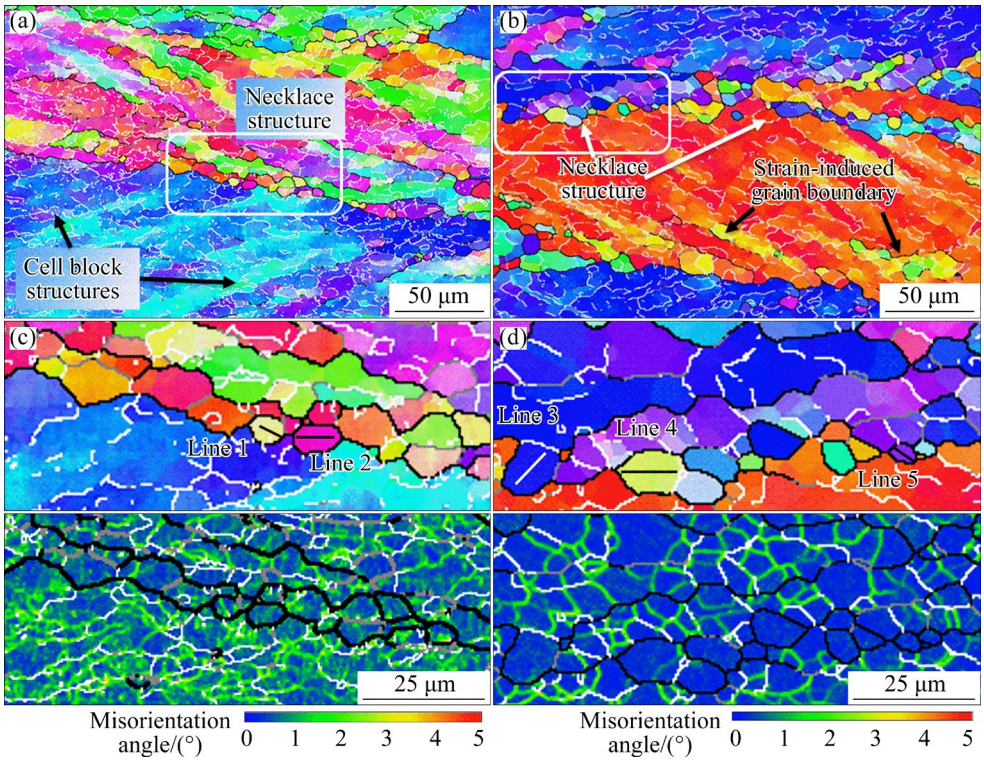

Fig. 10 Necklace structures formed under different hot deformation conditions: (a) Magnified Region B in Fig. 3(e) of sample deformed at 1150 °C, 0.01 s^{-1}; (b) Magnified Region E in Fig. 7(c) of sample deformed at 1350 °C, 1 s^{-1}; (c) KAM map of necklace structure in (a); (d) KAM map of necklace structure in (b)

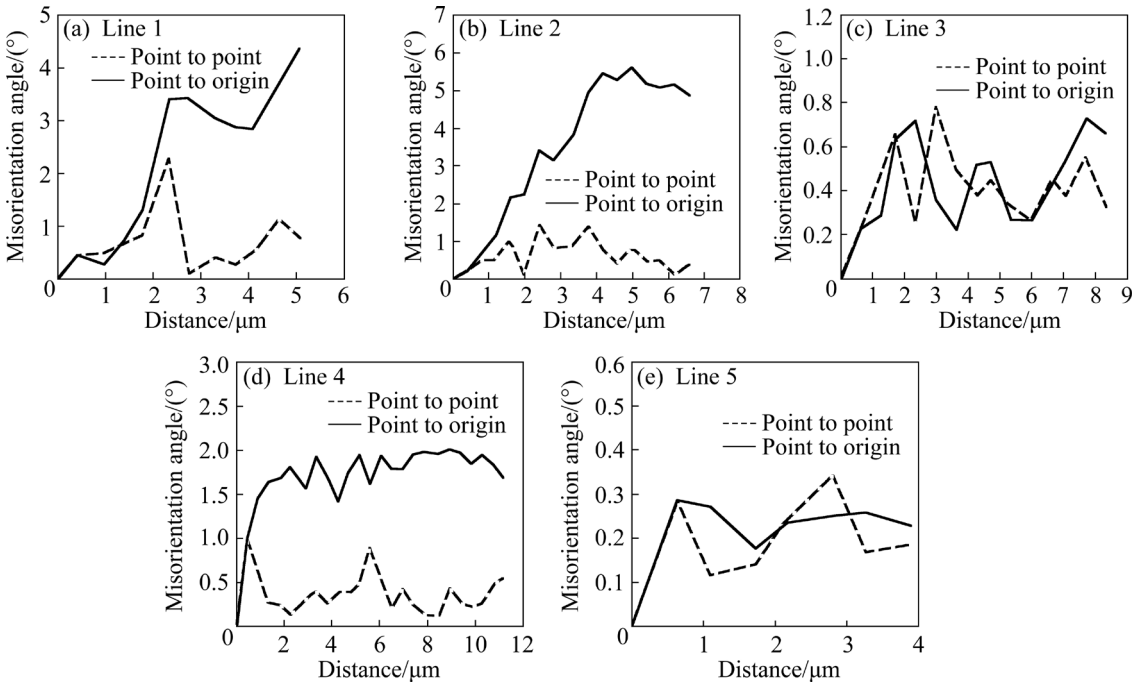

Fig. 11 Corresponding misorientation gradients of Lines 1 (a), 2 (b), 3 (c), 4 (d) and 5 (e) in Figs. 10(c, d)

Compared with the specimen deformed at a high strain rate, the specimen deformed at 1150 °C, 0.01 s^{-1} has a relatively high level of freedom in dislocation rearrangement, cell block structures enclosed or semienclosed by LAGBs can be seen in the initial grain (marked by black arrows in Fig. 10(a)), and those structure regions usually include low- to medium-angle subboundaries where the misorientation angles are conjointly accommodated. Relatively uniform deformation makes the strain concentrated in the region of the initial grain boundary, and subgrains near the grain boundary more easily transform into DRX grains via progressive lattice rotation. This kind of CDRX is reported by progressive lattice rotation near grain boundaries (LRGBs), also known as recovery-assisted DRX (DRV-assisted DRX) [23,24].

In addition to the DRX mode mentioned above, there are other DRX modes in the necklace structure. The prominent characteristics of bulging can be found in grains containing Line 3 and Line 5, and there are small stored energy gradients in these grains from the KAM map in Fig. 10(d). This phenomenon indicates that the bulging part conforms to the formation characteristics of DDRX, so DDRX also participates in the formation of necklace structures in the sample deformed at 1350 °C, 1 s^{-1}.

The necklace structure not only is formed at the initial grain boundary but also gradually develops toward the interior of the deformed grain. There are some strain-induced grain boundaries in the deformed grains, as marked by black arrows in Fig. 10(b), which can serve as regions for the formation of necklace structures.

Many grains with the characteristics of bulging in the necklace structure are not fully bound by HAGBs, and most of the grains in the necklace structure contain large interior misorientation accumulations (≥2°). Hence, it is reasonable to believe that LRGBs-assisted DRX is the dominant mechanism at 1350 °C, 1 s^{-1} and that DDRX is the secondary mechanism for forming necklace structures.

Figure 12 shows origin-to-origin misorientation of Lines 1−3 in Fig. 7(e). The cumulative misorientations can easily exceed 15° in a smaller range relative to the initial grains, indicating that the misorientation accumulates and that progressive subgrain rotation has been well developed [16]. The LAGBs in the initial grains are dispersed, dividing the initial grain into several subgrains, such as Region F in Fig. 7(e). This type of DRX is traditional CDRX, i.e., CDRX by homogeneous increase in misorientation (HIM), which relies on continuously progressive rotation of subgrains [25]. If the

specimen continues to deform, these subgrains surrounded or semisurrounded by LAGBs are eventually enclosed by HAGBs.

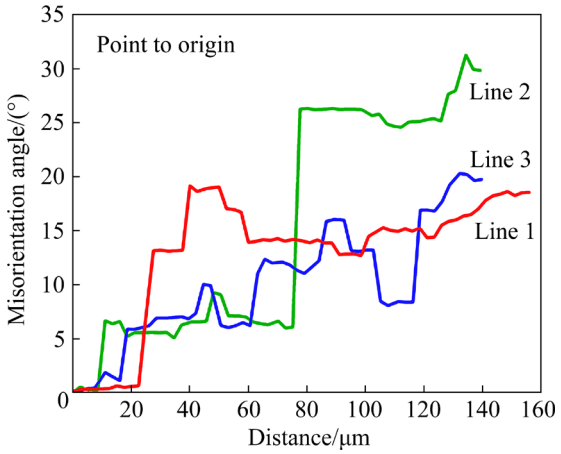

Fig. 12 Misorientation gradient measured along Lines 1, 2 and 3 in Fig. 7(e)

Due to the high deformation temperature and low strain rate, some grains are fully compressed, and many brick-like structures are formed in the microstructure. The formation of brick-like structures consumes many dislocations, as shown in Fig. 13(a). The initial grain boundary is still straight because the dislocation density in the grain is too low to generate bulging, which is consistent with the result of the KAM map of the region shown in Fig. 13(b).

The brick-like structure is a main feature of GDRX, and subgrains in brick-like structures have similar crystallographic orientations. If the parallel HAGBs are very close to each other and approach enough, the microstructure tends to collapse due to surface tension at triple points, and then "pinch-off" occurs, as marked by the white arrow in Fig. 13(a). Similarly, GDRX occurs at the extremities of deformed grains, marked by black arrows in Fig. 7(e) [26].

3.5 Effects of strain and strain rate on microstructure evolution of Pt−10Ir alloy

To investigate the DRX mechanisms influenced by the strain and strain rate, 1350 °C was chosen as the study temperature, and the grain boundary maps are shown in Figs. 14 and 15. Green lines indicate misorientation between 2° and 10°, red lines indicate misorientation between 10° and 15°, and black lines indicate misorientation larger than 15°.

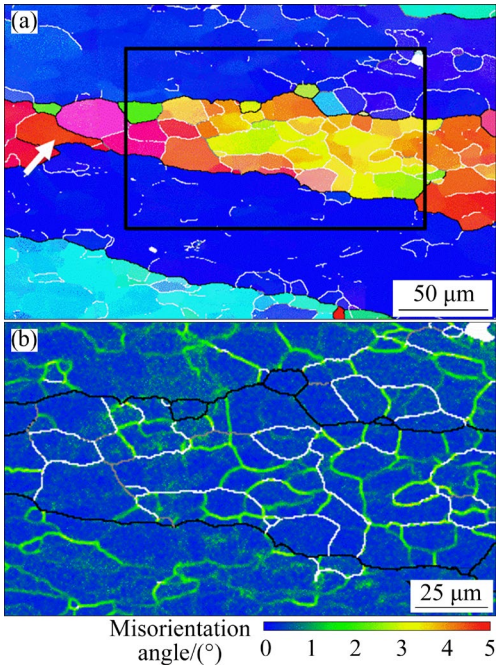

Fig. 13 Magnified Region G (a) in Fig. 7(e); KAM map of region marked by black box (b) in (a)

Figures 14(a−f) show the grain boundary maps deformed at different strains when the strain rates are 1 s^{-1} and 0.01 s^{-1}. Figures 14(g, h) show the misorientation distribution of the grain boundary.

At a constant strain rate of 1 s^{-1}, the local temperature rises due to the adiabatic heating effect, the impact of SIBM is promoted, and grain boundary bulging can be detected in Fig. 14(a). In addition, many LAGBs are produced in the deformed grains when the strain is relatively low. Figure 14(g) shows that LAGBs account for the highest proportion when the strain is 0.35. Some DRX grains and necklace structures are formed through the growth of subgrains located at the mantle regions situated along the initial grain boundaries, and they have higher misorientation gradients compared with the inside of the initial grains, marked by black arrows in Fig. 14(a). The formation of higher misorientation gradients should be the result of strain partitioning during plastic deformation, which results in a misfit in strain between the inside and outside a deformed grain. The misfit can be adjusted at the interface through local shear deformation and boundary sliding, so the misorientation of subboundaries near the mantle regions increases quickly [27,28]. As the strain increases to 0.7, the proportion of HAGBs increases

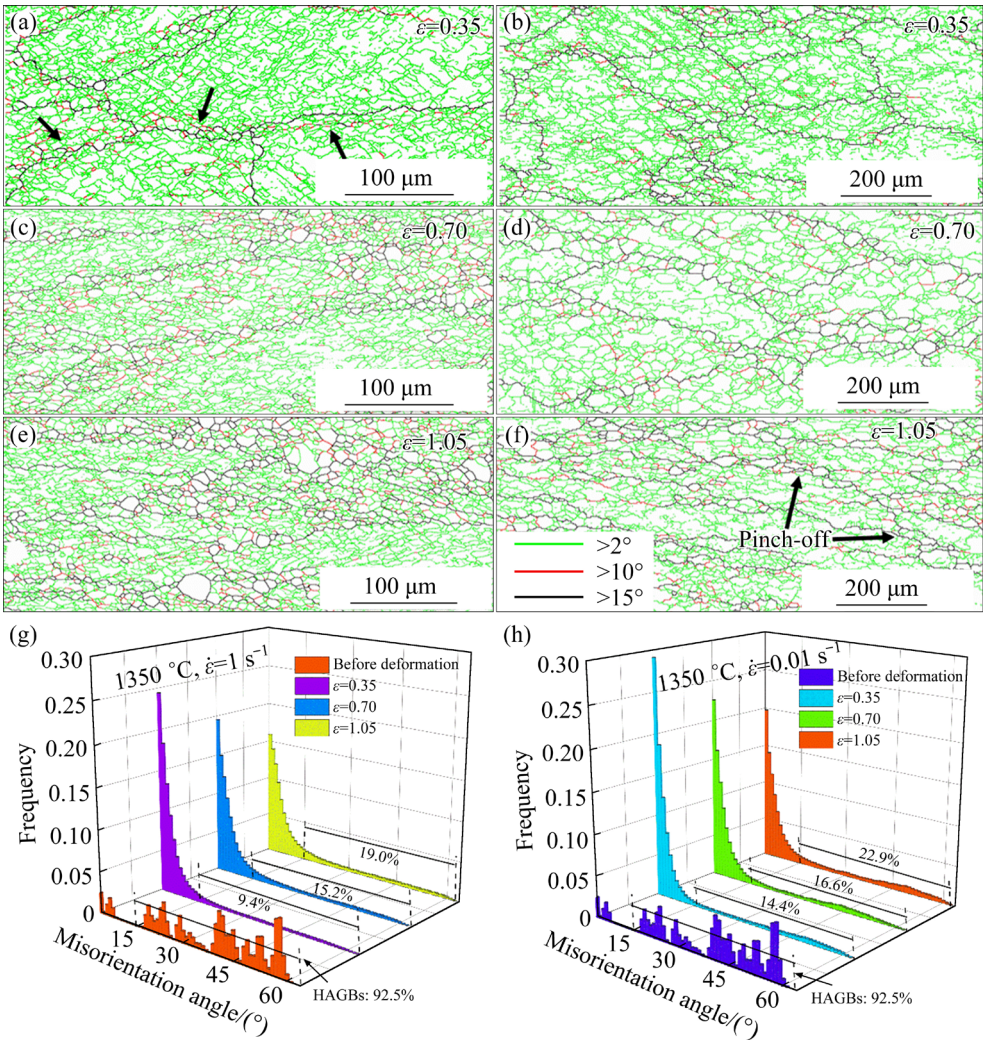

Fig. 14 Grain boundary maps of samples deformed at different strains: (a, c, e) With strain rate of $1 s^{-1}$; (b, d, f) With strain rate of 0.01 s^{-1}; (g) Misorientation angle distribution of samples deformed at 1350 °C, 1 s^{-1}; (h) Misorientation angle distribution of samples deformed at 1350 °C, 0.01 s^{-1}

to 15.2%. Moreover, the proportion of HAGBs reaches the highest of 19%, and the microstructure is almost covered by necklace structures when the strain increases to 1.05. At the same time, the proportion of LAGBs continues to decrease with increasing strain due to the fast conversion speed from LAGBs to HAGBs. At a high strain rate of 1 s^{-1}, DRX can be promoted by increasing strain. Both DDRX and CDRX by LRGBs are positively developed especially the latter.

The microstructure deformed at a lower strain rate of 0.01 s^{-1} is similar to that at a high strain rate of 1 s^{-1} when the strain is 0.35. However, there is no collection of MAGBs near the initial grain boundaries. A long deformation time makes the effect of DRV more sufficient, hindering the significantly from 16.6% to 22.9% with increasing accumulation of dislocations from conducting DDRX [23]. Well-developed subgrain structures with LAGBs can be observed in the initial grains shown in Fig. 14(d) when the strain is 0.7, and some of their boundaries gradually develop into MAGBs and HAGBs. CDRX is characterized by much slower kinetics than DDRX led by SIBM, and the migration rate of grain boundaries involved in traditional CDRX is 3 orders of magnitude smaller than that involved in DDRX [29,30]. As the strain continues to increase to 1.05, the grain gradually changes to a lamellar microstructure, LAGBs and MAGBs gradually separate large deformed grains into brick-like subgrains, the “pinch-off” is promoted and GDRX grain is well developed. From Fig. 14(h), the proportion of HAGBs increases strain. Although DRV is still the primary dynamic

softening mechanism, the proportion of DRX in the softening process increases because GDRX is effectively active by severe plastic deformation.

Figure 15 shows the influence of different strain rates on the grain boundary distribution at a fixed temperature of 1350 °C and a strain of 0.7. The size of the subgrains increases obviously with decreasing strain rate, as shown in Figs. 15(a−c), mainly because the extended deformation time

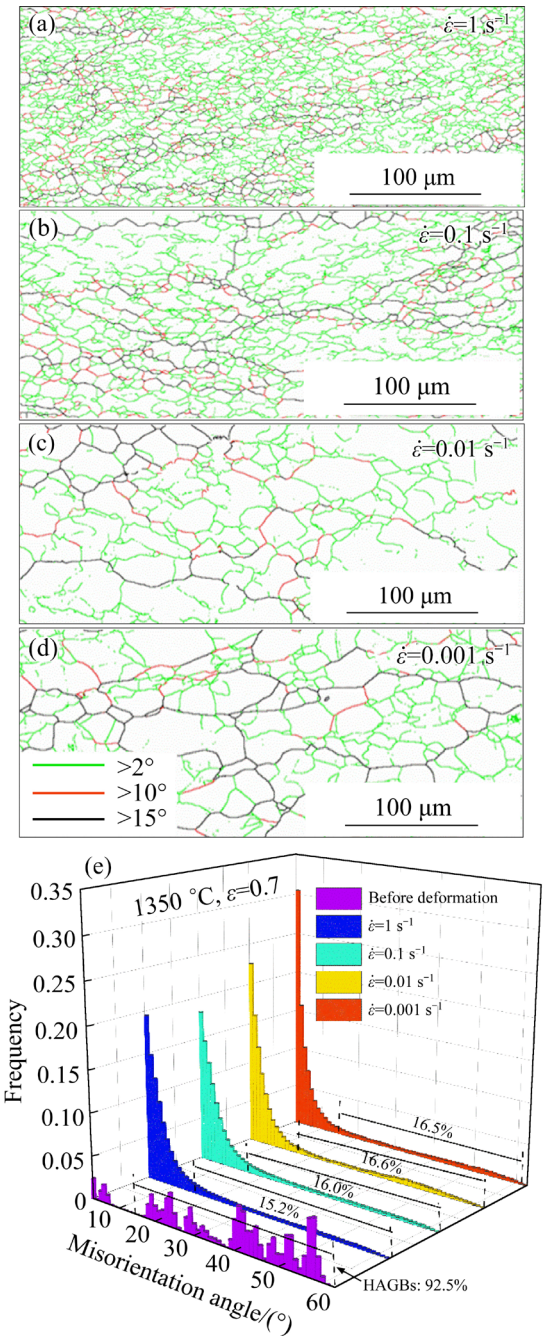

Fig. 15 Grain boundary maps in samples deformed at 1350 °C and strain of 0.7 with strain rate of 1 s^{-1} (a), 0.1 s^{-1} (b), 0.01 s^{-1} (c) and 0.001 s^{-1} (d); misorientation angle distribution of samples deformed at 1350 °C under different strain rates (e)

gives the subgrain a longer growth time, but the proportion of HAGBs only increases from 15.2% to 16.6%. The main reason for the insignificant numerical changes in HAGBs is that a lower strain rate increases the kinetic energy of atoms, so the dislocation movement is stronger, and most of the energy is consumed for microstructure recovery [15]. The microstructure deformed at a strain rate of 0.001 s^{-1} is the same as that at 0.01 s^{-1}, indicating that the DRV tends to be saturated. In other words, when the strain rate is lower than 0.01 s^{-1}, the effect of DRV does not increase with decreasing strain rate.

It is remarkable that with the decrease in the strain rate from 1 to 0.001 s^{-1}, the proportions of LAGBs show an upward trend, while the proportions of MAGBs represent a downward trend. At high strain rates, the transition from LAGBs to MAGBs is relatively high, and adiabatic temperature rise at high strain rates can lead to increased grain boundary mobility, making LAGBs more prone to increased misorientation [31,32]. LAGBs almost transform into HAGBs via SIBM under high strain rates and strains. Meanwhile, with the extension of deformation time, CDRX and GDRX are promoted.

3.6 Illustration of main DRX mechanism of Pt−10Ir alloy

During hot deformation of the Pt−10Ir alloy, two main DRX mechanisms can participate in dynamic softening: CDRX and GDRX. A schematic for the main DRX under different conditions is portrayed in Fig. 16.

Figure 16(a) shows the microshear bands (MSBs) assisted CDRX, which relies on some fixed oriented grains. These grains show a strong propensity to split by deformation bands [33]. If fewer slip systems in the grain are activated during deformation, a banded structure is formed, especially when deformed at low temperature and high strain rate [34,35]. These banded structures are not crystallographically related to the initial grains, which is beneficial to partitioning the total strain to make different regions undergo different strains, and it is energetically favorable to achieve macroscopically imposed shape change [17,33]. At the early deformation stage, some strain-induced LAGBs are generated from dislocation arrangement

along the shear direction [26,36]. With the low to medium strain, via the MAGB stage, the deformation band composed of strain-induced HAGBs is generated from LAGBs in the shear direction, and accompanied by the subdivision of transverse LAGBs. In the end, continuous strain results in the evolution of fine grains to separate from the deformation band [9].

Figure 16(b) shows the CDRX by LRGBs. This kind of CDRX relies on DRV to form well-defined subgrains in the grain boundary region [23]. DRV occurs when the strain is low, and the climb and cross-slip of dislocations are more active at the initial grain boundary because of the stress concentration [21]. Although SIBM occurs, dislocations are difficult to accumulate, and the dislocation density near the initial grain boundary may not be enough to lead to bulging. As seen in Fig. 8(a, b) and Fig. 9, the accumulated dislocation density in the SIBM regions is consumed, resulting in the formation of subgrain coalescence. The subgrains near the SIBM regions that deviate from their initial grains preferentially transform into DRX grains by subgrain rotation [28,37,38]. The DRX mechanism occurs not only along grain boundaries but also inside the grains, and such a process repeatedly occurs inside the initial grains [39]. This kind of DRX is the dominant DRX mechanism of the Pt−10Ir alloy.

CDRX by HIM is displayed in Fig. 16(c). This conventional CDRX relies on a high deformation temperature and low strain rate to form a homogeneous microstructure [5,40]. Due to the low strain rate, there is sufficient time for DRV in deformed microstructure. Dislocation cells are formed in the initial grains with increasing strain. With the annihilation and arrangement of dislocations, these dislocation cells can form equiaxed subgrains semienclosed by LAGBs, and then those subgrains continuously absorb deformation energy to form new grains through subgrain rotations [7,26].

The GDRX shown in Fig. 16(d) is largely dependent on the role of DRV [5], so it is more likely to occur in alloys with high stacking fault energy. Uniform deformation fully compresses the initial grains, the HAGBs of the deformed grain tend to be parallel, and some brick-like subgrains are formed through thinning of the grain width. When those HAGBs approach 1−2 times the subgrain size, the boundaries collapse due to surface tension, the “pinch-off” process occurs, and GDRX grains are produced from this process [22,41]. GDRX could also occur in a part of the DRX grains formed by LRGBs located at the mantle regions [7].

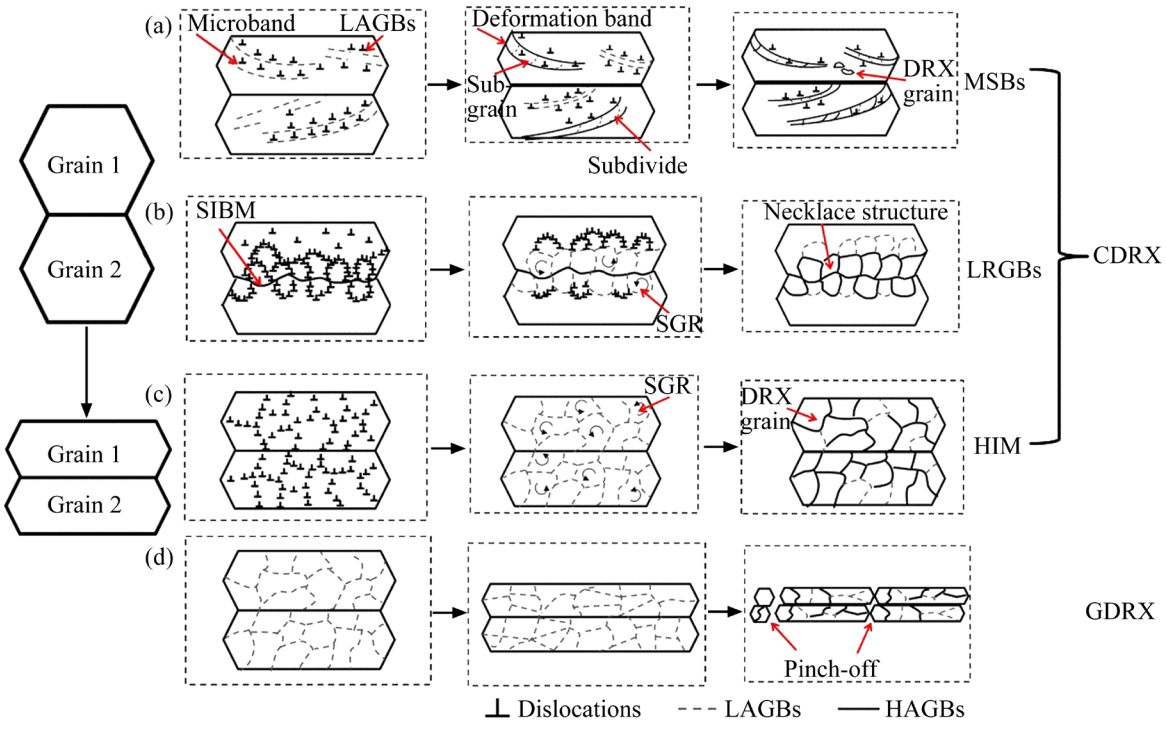

Fig. 16 Schematic of main DRX mechanisms in Pt−10Ir alloy (SGR: Subgrain rotation)

4 Conclusions

(1) At low deformation temperatures (950−1150 °C), microbands and deformation bands resulting from strain localization are promoted. Two kinds of CDRX coordinate hot deformation: DRX by LRGBs and MSBs assisted DRX. The dynamic softening is weak, and it is difficult to offset the work hardening, resulting in no obvious softening in the flow curves.

(2) The kinetics of microstructure evolution at high deformation temperatures (1250−1350 °C) is DRV. CDRX by LRGBs is obviously increased because of intense DRV, and many necklace structures near the deformed grains are produced at high strain rates. At low strain rates, the microstructure has uniform deformation and noticeable flattening, CDRX by HIM and GDRX are enhanced, and the flow curves show significant softening.

(3) With increasing strain, both CDRX and GDRX are promoted. Grain boundary bulging and CDRX by LRGBs are both increased at high strain rates, which is beneficial to producing fine microstructures. At low strain rates, the deformed grains form an obvious layered structure and the effect of "pinch-off" is promoted, so GDRX is obviously enhanced, which has a positive effect on the formation of a uniform microstructure.

CRediT authorship contribution statement

Xin-pei ZHANG: Writing − Original draft, Writing − Review & editing; **Jun-jie HE:** Investigation, Writing − Review & editing, Project administration, Funding acquisition; **Lin PI:** Investigation; **Quan FU:** Investigation; **Wen-yan ZHOU:** Project administration, Funding acquisition; **Jun CHENG:** Investigation; **Sheng-wen BAI:** Investigation; **Xuan ZHOU:** Investigation; **Yi LIU:** Project administration, Funding acquisition; **Yong MAO:** Writing − Review & editing, Project administration, Funding acquisition.

Declaration of competing interest

The authors declare that they have no known competing financial interests or personal relationships that could have appeared to influence the work reported in this paper.

Acknowledgments

The authors are grateful for the financial supports from the National Natural Science Foundation of China (Nos. 52161023, 51901204), Science and Technology Project of Yunnan Precious Metal Laboratory, China (No. YPML–2023050208), Yunnan Science and Technology Planning Project, China (Nos. 202201AU070010, 202301AT070276, 202302AB080008, 202303AA080001), and Postgraduate Research and Innovation Foundation of Yunnan University, China (No. 2021Y338).

References

[1] YAO Xin, MAO Yong, GUO Ya-fang. Effects of alloying elements on the generalised stacking fault energies of Pt: A first-principles study [J]. Philosophical Magazine, 2021, 101: 1033−1047.

[2] WANG Sai-bei, SUN Yong, WANG Song, PENG Ming-jun, LIU Man-men, DUAN Yong-hua, CHEN Yong-tai, YANG You-cai, CHEN Song, LI Ai-kun, XIE Ming. Effect of yttrium on the microstructure and properties of Pt−Ir electrical contact materials [C]//IOP Conference Series: Materials Science and Engineering, 2017, 250: 012017.

[3] GUI Yun-wei, OUYANG Ling-xiao, XUE Yi-bei, LI Quan-an. Effect of thermo-mechanical processing parameters on the dynamic restoration mechanism in an Mg−4Y−2Nd−1Sm−0.5Zr alloy during hot compression [J]. Journal of Materials Science & Technology, 2021, 90: 205−224.

[4] ZHANG Jian-yang, XU Bin, HAQ TARIQ N, SUN Ming-yue, LI Dian-zhong, LI Yi-yi. Microstructure evolutions and interfacial bonding behavior of Ni-based superalloys during solid state plastic deformation bonding [J]. Journal of Materials Science & Technology, 2020, 46: 1−11.

[5] YIN Xiang-qian, PARK Chan-hee, LI Yan-feng, YE Wen-jun, ZUO Yu-ting, LEE Sang-won, YEOM Jong-taek, MI Xu-jun. Mechanism of continuous dynamic recrystallization in a 50Ti−47Ni−3Fe shape memory alloy during hot compressive deformation [J]. Journal of Alloys and Compounds, 2017, 693: 426−431.

[6] CHAMANFAR A, ALAMOUDI M T, NANNINGA N E, MISIOLEK W Z. Analysis of flow stress and microstructure during hot compression of 6099 aluminum alloy (AA6099) [J]. Materials Science and Engineering A, 2019, 743: 684−696.

[7] LI Jia-chen, WU Xiao-dong, CAO Ling-fei, LIAO Bin, WANG Yi-chang, LIU Qing. Hot deformation and dynamic recrystallization in Al−Mg−Si alloy [J]. Materials Characterization, 2021, 173: 110976.

[8] SUN J Z, LI M Q, LI H. Interaction effect between alpha and beta phases based on dynamic recrystallization of isothermally compressed Ti−5Al−2Sn−2Zr−4Mo−4Cr with basketweave microstructure [J]. Journal of Alloys and Compounds, 2017, 692: 403−412.

[9] YANUSHKEVICH Z, BELYAKOV A, KAIBYSHEV R. Microstructural evolution of a 304-type austenitic stainless steel during rolling at temperatures of 773−1273 K [J]. Acta Materialia, 2015, 82: 244−254.

[10] CHEN Zhao-qi, XU Li-juan, CAO Shou-zhen, YANG Jian-kai, ZHENG Yun-fei, XIAO Shu-long, TIAN Jing, CHEN

Yu-yong. Characterization of hot deformation and microstructure evolution of a new metastable β titanium alloy [J]. Transactions of Nonferrous Metals Society of China, 2022, 32: 1513−1529.

[11] MAO Yong, ZHU Dan-li, HE Jun-jie, DENG Chao, SUN Ying-jie, XUE Guang-jie, YU Heng-fei, WANG Chen. Hot deformation behavior and related microstructure evolution in Au–Sn eutectic multilayers [J]. Transactions of Nonferrous Metals Society of China, 2021, 31: 1700−1716.

[12] GAN Yi, HU Li, SHI Lai-xin, CHEN Qiang, LI Ming-ao, XIANG Lin, ZHOU Tao. Effect of AlLi phase on deformation behavior and dynamic recrystallization of Mg−Li alloy during hot compression [J]. Transactions of Nonferrous Metals Society of China, 2023, 33: 1373−1384.

[13] NAGAUMI H, QIN Jian, YU Cheng-bin, WANG Xiao-guo, WANG Lin-sheng. Quantitative analysis of influence of α-Al(MnFeCr)Si dispersoids on hot deformation and microstructural evolution of Al−Mg−Si alloys [J]. Transactions of Nonferrous Metals Society of China, 2022, 32: 1805−1821.

[14] HUANG Liang, LI Chang-min, LI Cheng-lin, HUI Song-xiao, YU Yang, ZHAO Ming-jie, GUO Shi-qi, LI Jian-jun. Research progress on microstructure evolution and hot processing maps of high strength β titanium alloys during hot deformation [J]. Transactions of Nonferrous Metals Society of China, 2022, 32: 3835−3859.

[15] LI Peng-wei, LI Hui-zhong, HUANG Lan, LIANG Xiao-peng, ZHU Ze-xiao. Characterization of hot deformation behavior of AA2014 forging aluminum alloy using processing map [J]. Transactions of Nonferrous Metals Society of China, 2017, 27: 1677−1688.

[16] CHEN Ke, WU Jie-qiong, SHI Hui, CHEN Xing-fang, SHEN Zhi, ZHANG Mei, ZHANG Lan-ting, SHAN Ai-dang. Transition of deformation behavior and its related microstructure evolution in Nimonic 80A under hot-to-warm working [J]. Materials Characterization, 2015, 106: 175−184.

[17] HAGHDADI N, PRIMIG S, ANNASAMY M, CIZEK P, HODGSON P D, FABIJANIC D M. On the hot-worked microstructure of a face-centered cubic $Al_{0.3}CoCrFeNi$ high entropy alloy [J]. Scripta Materialia, 2020, 178: 144−149.

[18] TAYLOR A S, CIZEK P, HODGSON P D. Orientation dependence of the substructure characteristics in a Ni−30Fe austenitic model alloy deformed in hot plane strain compression [J]. Acta Materialia, 2012, 60: 1548−1569.

[19] ZHONG Xi-ting, WANG Lei, HUANG Lin-ke, LIU Feng. Transition of dynamic recrystallization mechanism during hot deformation of Incoloy 028 alloy [J]. Journal of Materials Science & Technology, 2020, 42: 241−253.

[20] KHATAMI-HAMEDANI H, ZAREI-HANZAKI A, ABEDI H R, ANOUSHE A S, KARJALAINEN L P. Dynamic restoration of the ferrite and austenite phases during hot compressive deformation of a lean duplex stainless steel [J]. Materials Science and Engineering A, 2020, 788: 139400.

[21] HAGHDADI N, CIZEK P, BELADI H, HODGSON P D. The austenite microstructure evolution in a duplex stainless steel subjected to hot deformation [J]. Philosophical Magazine, 2017, 97: 1209−1237.

[22] ZENG X, FAN X G, LI H W, ZHAN M, LI S H. Grain morphology related microstructural developments in bulk deformation of 2219 aluminum alloy sheet at elevated temperature [J]. Materials Science and Engineering A, 2019, 760: 328−338.

[23] HUANG K, LOGÉ R E. A review of dynamic recrystallization phenomena in metallic materials [J]. Materials & Design, 2016, 111: 548−574.

[24] LI Wang, Deng YUE, GU Jin-bo, MU Wang-zhong, LI Jingyuan. Correlation of microstructure and dynamic softening mechanism of UNS S32101 duplex stainless steel during elevated temperature tensile testing [J]. Materials Science and Engineering A, 2022, 855: 143868.

[25] WANG S, LUO J R, HOU L G, ZHANG J S, ZHUANG L Z. Physically based constitutive analysis and microstructural evolution of AA7050 aluminum alloy during hot compression [J]. Materials & Design, 2016, 107: 277−289.

[26] WANG M J, SUN C Y, FU M W, LIU Z L, QIAN L Y. Study on the dynamic recrystallization mechanisms of Inconel 740 superalloy during hot deformation [J]. Journal of Alloys and Compounds, 2020, 820: 153325.

[27] MEHTONEN S V, KARJALAINEN L P, PORTER D A. Hot deformation behavior and microstructure evolution of a stabilized high-Cr ferritic stainless steel [J]. Materials Science and Engineering A, 2013, 571: 1−12.

[28] DUDOVA N, BELYAKOV A, SAKAI T, KAIBYSHEV R. Dynamic recrystallization mechanisms operating in a Ni−20%Cr alloy under hot-to-warm working [J]. Acta Materialia, 2010, 58: 3624−3632.

[29] DOHERTY R D, HUGHES D A, HUMPHREYS F J, JONAS J J, JENSEN D J, KASSNER M E, KING W E, MCNELLEY T R, MCQUEEN H J, ROLLETT A D. Current issues in recrystallization: A review [J]. Materials Science and Engineering A, 1997, 238: 219−274.

[30] SAKAI T, BELYAKOV A, KAIBYSHEV R, MIURA H, JONAS J J. Dynamic and post-dynamic recrystallization under hot, cold and severe plastic deformation conditions [J]. Progress in Materials Science, 2014, 60: 130−207.

[31] LIAO Bin, WU Xiao-dong, CAO Ling-fei, HUANG Guang-jie, WANG Zhen-gan, LIU Qing. The microstructural evolution of aluminum alloy 7055 manufactured by hot thermo-mechanical process [J]. Journal of Alloys and Compounds, 2019, 796: 103−110.

[32] NAYAN N, MURTY S V S N, CHHANGANI S, PRAKASH A, PRASAD M J N V, SAMAJDAR I. Effect of temperature and strain rate on hot deformation behavior and microstructure of Al−Cu−Li alloy [J]. Journal of Alloys and Compounds, 2017, 723: 548−558.

[33] PODDAR D, CIZEK P, BELADI H, HODGSON P D. Microstructure characteristics of the ⟨111⟩ oriented grains in a Fe−30Ni−Nb model austenitic steel deformed in hot uniaxial compression [J]. Materials Characterization, 2016, 118: 382−396.

[34] JIANG Jing-yu, JIANG Feng, HUANG Hong-feng, ZHANG Meng-han, TANG Zhong-qin, TONG Meng-meng. Hot deformation analysis and microstructure evolution of Al−Mg−Mn−Sc−Zr alloy by isothermal compression [J]. Journal of Alloys and Compounds, 2021, 858: 157655.

[35] LIU Lei, WU Yun-xin, GONG Hai, LI Shuang, AHMAD A S. A physically based constitutive model and continuous dynamic recrystallization behavior analysis of 2219

aluminum alloy during hot deformation process [J]. Materials, 2018, 11: 1443.
[36] ARUN BABU K, MOZUMDER Y H, ATHREYA C N, SARMA V S, MANDAL S. Implication of initial grain size on DRX mechanism and grain refinement in super-304H SS in a wide range of strain rates during large-strain hot deformation [J]. Materials Science and Engineering A, 2022, 832: 142269.
[37] HAGHDADI N, CIZEK P, BELADI H, HODGSON P D. A novel high-strain-rate ferrite dynamic softening mechanism facilitated by the interphase in the austenite/ferrite microstructure [J]. Acta Materialia, 2017, 126: 44−57.
[38] CIZEK P. The microstructure evolution and softening processes during high-temperature deformation of a 21Cr−10Ni−3Mo duplex stainless steel [J]. Acta Materialia, 2016, 106: 129−143.
[39] QIANG Feng-ming, BOUZY E, KOU Hong-chao, ZHANG Yu-dong, WANG Ling-ling, LI Jin-shan. Grain fragmentation associated continuous dynamic recrystallization (CDRX) of hexagonal structure during uniaxial isothermal compression: High-temperature α phase in TiAl alloys [J]. Intermetallics, 2021, 129: 107028.
[40] DONG Cui-ge, WANG Ri-chu, WANG Xiao-feng, ZHOU Lang-ya. Hot deformation characteristics and microstructure evolution of SiC_p/Al2014 composite fabricated by powder metallurgy [J]. Journal of Materials Engineering and Performance, 2022, 31: 221−229.
[41] YANG Sheng-li, SHEN Jian, ZHANG Yong-an, LI Zhi-hui, LI Xi-wu, HUANG Shu-hui, XIONG Bai-qing. Processing maps and microstructural evolution of Al−Cu−Li alloy during hot deformation [J]. Rare Metals, 2019, 38(12): 1136−1143.

贵金属合金 Pt−10Ir 的流变行为及动态软化机制

张心培[1]，何俊杰[1]，皮 琳[1]，付 全[2]，周文艳[3,4]，程 军[5]，白生文[6]，周 璇[1]，刘 毅[2]，毛 勇[1]

1. 云南大学 材料与能源学院 材料基因工程研究中心，昆明 650091；
2. 贵研铂业股份有限公司 云南贵金属实验室有限公司 昆明贵研新材料科技有限公司，昆明 650106；
3. 昆明贵金属研究所，昆明 650106；
4. 贵研铂业股份有限公司 稀贵金属综合利用新技术国家重点实验室，昆明 650106；
5. 西北有色金属研究院 陕西省医用金属材料重点实验室，西安 710016；
6. 重庆大学 材料科学与工程学院，重庆 400044

摘 要：研究了 Pt−10Ir 合金在大范围变形参数下的热变形行为。在较低变形温度(950−1150 ℃)下，Pt−10Ir 合金的软化机制主要是动态回复。此外，通过晶界处渐进晶格旋转的动态再结晶及微剪切带辅助的动态再结晶也会协调热变形过程，但由于产生的动态再结晶晶粒有限，动态软化难以抵消应变硬化的作用。在较高变形温度(1250−1350 ℃)下，主要产生 3 种与应变速率有关的动态再结晶：晶界处渐进晶格旋转的动态再结晶、取向差均匀增加的动态再结晶及几何动态再结晶。随着应变量的增加，在高应变速率下，晶界处渐进晶格旋转的动态再结晶的作用逐渐得到加强；在低应变速率下，晶粒“夹断”效应增强，有利于形成均匀、细小的显微组织。

关键词：铂合金；热变形；显微组织演化；动态回复；动态再结晶

(Edited by Bing YANG)